ADVANCED FUNCTIONAL MATERIALS

Supporting Information

for *Adv. Funct. Mater.,* DOI: 10.1002/adfm.202203966

Chemotherapeutics and CAR-T Cell-Based Immunotherapeutics Screening on a 3D Bioprinted Vascularized Breast Tumor Model

*Madhuri Dey, Myoung Hwan Kim, Mikail Dogan, Momoka Nagamine, Lina Kozhaya, Nazmiye Celik, Derya Unutmaz, and Ibrahim T. Ozbolat**

Supporting Information for

"**Chemotherapeutics and CAR-T cell-based immunotherapeutics screening on a 3D bioprinted vascularized breast tumor model"**

Authors: Madhuri Dey, Myoung Hwan Kim, Mikail Dogan, Momoka Nagamine, Lina Kozhaya, Nazmiye Celik, Derya Unutmaz, Ibrahim T. Ozbolat

Results

Evaluation of tumor spheroid and composite hydrogel properties for precise positioning of the tumor spheroids

Aspiration-assisted bioprinting was utilized for precise positioning of tumor spheroids, which involved aspirating tumor spheroids and placing them at desired locations into a biomimetic matrix. Thus, it was crucial to assess the structural and mechanical properties of spheroids for successful bioprinting. In this study, first, we sought to compare three different types of tumor spheroids, homocellular spheroids formed by MDA-MB-231 cells (MDA-MB-231-only), co-cultured spheroids formed by HUVECs and MDA-MB-231 cells (H231), and a third type formed by a combination of HUVECs, MDA-MB-231 cells and HDFs (H231F). These three different types of spheroids exhibited not only distinct morphological differences but also contrasting mechanical properties. MDA-MB-231-only spheroids were unable to withstand the back pressure and experienced a major deformation in their structure due to aspiration (Fig. S1A1). Eventually, MDA-MB-231-only spheroids disaggregated and were completely aspirated, indicating their extremely weak mechanical properties and low structural integrity; thus, unsuitable for 3D bioprinting. Next, on repeating the same process for H231 and H231F spheroids, the latter exhibited the highest structural integrity as little to no deformation occurred in H231F spheroids even after 10 min of exposure to back pressure. On measuring the elastic

modulus of all spheroid types, H231F exhibited the highest average modulus, ~160 Pa, as compared to H231, which had an average modulus of ~105 Pa (Fig. S1A2). We were unable to get a definite elastic modulus value for MDA-MB-231-only spheroids as they completely lost their structural integrity during elastic modulus measurement. Ultrastructural images of all spheroid types revealed a dense and compact morphology for H231F as compared to H231 and MDA-MB-231-only spheroids (Fig. S1A3). Thus, owing to their superior mechanical and structural integrity, and heterotypic nature mimicking tumor microenvironment, H231F spheroids were preferred for 3D bioprinting experiments. In order to identify the different cell types, the entire heterotypic H231F tumor spheroid, comprising of GFP^+ MDA-MB-231, $tdTomato^+$ HUVEC, was immunostained with PDGFR-α to identify the HDFs (Fig. S1B). Confocal Z-stack images were captured for these tumors, however, due to limited depth of penetration, we were unable to image the spheroid core for an accurate spatial analysis (Movie S5). Hence, the tumors were paraffin embedded and sectioned on a microtome. Tumor sections from the central region were chosen and immunostained with PDGFR-α antibody (Figs. S2). H231F sections revealed a heterogenous distribution of GFP^+ MDA-MB-231 cells throughout the tumor sections, whereas HUVECs and HDFs were comparatively homogenous in distribution (Fig. S2A2-E2).

αSMA expression in heterotypic H231F spheroids was evaluated and compared to homotypic MDA-MB-231-only and heterotypic H231 spheroids, all cultured under similar conditions for three days. All three types of spheroids stained positive for αSMA; however, there was a stronger signal on the heterotypic H231F spheroids (Fig. S3A). Similarly, picrosirius red staining of these spheroids exhibited a significantly higher collagen deposition for the

heterotypic H231F tumors as compared to that of the homotypic MDA-MB-231-only tumor as well as heterotypic H231 tumor spheroids (Fig. S3B1-B2)

Collagen and fibrin, both being abundantly present at a native tumor site, were incorporated in our study as the bioprinting substrate. Building on our previous study,[1] we incorporated 2 mg/ml collagen along with 3 mg/ml fibrinogen in this study (C2F3), to build the tumor microenvironment. In order to precisely position H231F spheroids in the composite C2F3 hydrogel, it was essential to conclude the entire bioprinting process prior to complete crosslinking of C2F3. Bioprinting inside a crosslinked hydrogel would result in irreversible gel deformation as C2F3 did not possess self-healing properties. Thus, to understand the rheological changes in C2F3 during bioprinting performed at RT (22 °C), a time sweep test was performed, first at RT, and then at 37 °C. A gradual increase in storage modulus was observed for C2F3 incubated at RT, for the first ~ 300 s (5 min) (Fig. S4A1). In contrast, a sharp increase in storage modulus was observed for C2F3 incubated at 37 °C, in the first few seconds itself. The storage modulus eventually acquired a constant value of ~100 Pa in ~ 20 min at both RT and 37 °C. This implied that incubating C2F3 at RT offered a time window of ~ 5 min to complete the bioprinting process before onset of crosslinking. Further, to understand if the rheological properties of C2F3 altered when finally incubated at 37 ºC after bioprinting, we performed a similar time sweep test at 37 ºC after the initial 20 min run at RT (Fig. S4A2). The storage modulus for C2F3 eventually recovered and reached a mean value of ~ 400 Pa, which closely matched that of C2F3 incubated at 37 ºC throughout. Additionally, storage modulus of the precursors C2 and F3 were significantly lower to that of composite C2F3 (Fig. S4A3). C2F3 also exhibited a significantly high relative stiffness, ~1211 Pa, as compared to the precursors C2, ~727 Pa, and F3, ~8 Pa (Fig. S4A4).

On optimizing both the matrix and tumor spheroid properties required for 3D bioprinting, bioprinting accuracy was also determined for H231F spheroids, which was measured to be ~50 µm (Fig. S4B). Additionally, the circularity of spheroids before and after bioprinting was also determined to be similar (~0.5) indicating that bioprinting had minimal effect on spheroid morphology (Fig. S4C).

Confirmation of the barrier function of the engineered vasculature

To confirm the barrier function of the engineered vasculature, the diffusional permeability was evaluated and compared with respect to non-endothelialized channels (empty). Non-endothelialized channels exhibited a significantly higher diffusion of fluorescein isothiocyanate (FITC)-conjugated dextran as compared to the endothelialized channels (Fig. S5A). Diffusional permeability for empty channels in C2F3 had a mean value of ~ $7x10^{-5}$ cm/s as compared to ~ $2x10^{-5}$ cm/s, for endothelialized channels. Additionally, CD31 staining of HUVECs in the endothelialized channel exhibited their uniform lining throughout the vasculature (Fig. S5B). H231F spheroids were bioprinted either proximal (at a distance of ~ 100 µm) or distal (~ 500 µm) to the endothelialized channel (vasculature).

Effects of chemotherapeutic drug doxorubicin, on tumor growth under static culture conditions

Doxorubicin was initially tested on static tumor cultures, which included free-standing spheroids and C2F3 encapsulated spheroids. Doxorubicin concentration was varied from 0.0001 to 100 µM and spheroids were treated with it for a period of 72 h. A non-treated group was used as control, containing only vehicle (0.1% DMSO). Herein, we tested the effect of this drug on two different

types of tumors, including MDA-MB-231-only and H231F spheroids. In particular, we aimed to assess if the presence of other cell types affected the drug response. As depicted in fluorescent images in Fig. S7A1, MDA-MB-231-only spheroids showed a significant reduction in GFP intensity for doxorubicin concentrations ranging from 1 to 100 µM. There was also a reduction in spheroid size for this concentration range, evident from the fluorescent images. Viability of spheroids was measured after a 72 h doxorubicin treatment to understand their dose-response behavior (Fig. S7A2). An IC_{50} value of ~ 0.51 µM was obtained for MDA-MB-231-only spheroids. Within a 95% confidence interval (C.I.), the IC_{50} range was predicted to be ~ 0.3 – 0.85 µM for MDA-MB-231-only spheroids. Similarly, heterotypic H231F spheroids were also treated with varying concentrations of doxorubicin for 72 h. As shown in Fig. S7B1, there was a reduction in GFP intensity for 1 - 100 µM. An IC_{50} value of ~ 0.65 µM was obtained from the dose response curve (Fig. S7B2). Additionally, within a 95% C.I., the IC_{50} range for H231F was predicted to be ~ 0.4 – 1.1 µM.

To understand the effect of extracellular matrix (ECM) on drug response of tumors, we encapsulated MDA-MB-231-only and H231F spheroids in C2F3, without any HDFs in the matrix. These spheroids were first cultured for a period of 3 days to allow them to grow in C2F3 and then varying concentrations of doxorubicin was introduced to these cultures for 72 h. As shown in Fig. S8, there was a significant reduction in GFP intensity for 10 and 100 µM doxorubicin treated spheroids, indicating extensive cell death. For 0.001 to 1 µM, there was also a reduction in tumor size and invasion, as compared to the non-treated or vehicle control groups. Additionally, we obtained an IC_{50} value of ~ 0.22 µM with an IC_{50} range of 0.12-0.3 µM (95% C.I.), which was much lower than the MDA-MB-231-only group in previous experiments, where free-standing tumors were directly exposed to doxorubicin. This observation suggested that

tumor-ECM interactions could affect drug outcomes. Interestingly, when H231F spheroids were encapsulated in C2F3 and treated with doxorubicin for 72 h, tumor viability ranged from ~88-97% for 0.0001 - 0.1 μM (Figs. S8B1-B2). Fluorescent images in Fig. S8B1 revealed that GFP intensity was most affected by 1, 10, and 100 μM concentrations. We also obtained a higher IC_{50} value of ~ 0.9 μM as compared to 0.2 μM for the MDA-MB-231-only spheroids encapsulated in C2F3. Similarly, an IC_{50} range of ~ 0.6 - 1.3 μM (95% C.I.) was obtained for H231F spheroids encapsulated in C2F3.

Engineering HER2-targeting CAR-T cells

In order to express anti HER2 CAR synthetic genes in primary CD8 T cells, we first designed a lentiviral CAR construct comprising a CD8α signal peptide, an anti-HER2 antibody single chain variable fragment (scFv), CD8 hinge domain, CD8 transmembrane domain, 41BB co-stimulatory domain and CD3 zeta (ζ) domain. The CAR cassette was designed to be co-expressed by LTR promoter with a red fluorescent protein (RFP) reporter via an internal ribosome entry site (IRES) (Fig. S10A). An anti-CD19 CAR construct was also designed by swapping the anti HER2 scFv with an anti CD19 counterpart. To express the CAR constructs and expand the cells, resting CD8 T cells were activated by anti CD3/CD28 bead-stimulation and transduced with lentiviruses encoding the CAR constructs one day after the stimulation. The cells were then cultured for 10 days in the presence of IL-2 and stained for surface anti HER2 expressions. A recombinant HER2-Fc protein was used to bind to anti HER2 part of the CAR on cell surface and a fluorescent conjugated anti-Fc antibody was used for flow cytometry staining.

Flow cytometry analysis showed that engineered CD8 T cells expressed anti HER2 scFv on their surface (Fig. S10B).

After confirming the CAR expression on CD8 T cells, we next designed a cytotoxicity assay to test the functionality of the CAR construct targeting HER2-expressing MDA-MB-231 cells (Fig. S10C). Three days after co-incubation, using flow cytometry analysis, we showed that anti-HER2 CD8 T cells were able to kill their targets efficiently (Fig S10D). These findings demonstrate the specific killing of HER2-expressing target cells by anti HER2 CAR-T cells.

Effects of anti HER2 CAR-T cells on distally bioprinted tumors under perfusion culture conditions

Tumor spheroids were bioprinted distally to the perfused vasculature and then subjected to a high density (3M) of aHER-2 CAR-T treatment (Fig. S13A). After 24h of perfusion, tumor volume for the distal tumors were similar to that of the non-treated (control) group as compared to proximal tumors (Fig. S13B). Additionally, significantly lower number of CAR-Ts were found near the distally-bioprinted tumors as compared to the proximal tumors (Fig S13C). Thus, we selected the proximally-bioprinted group for the rest of the study.

Supporting Figures

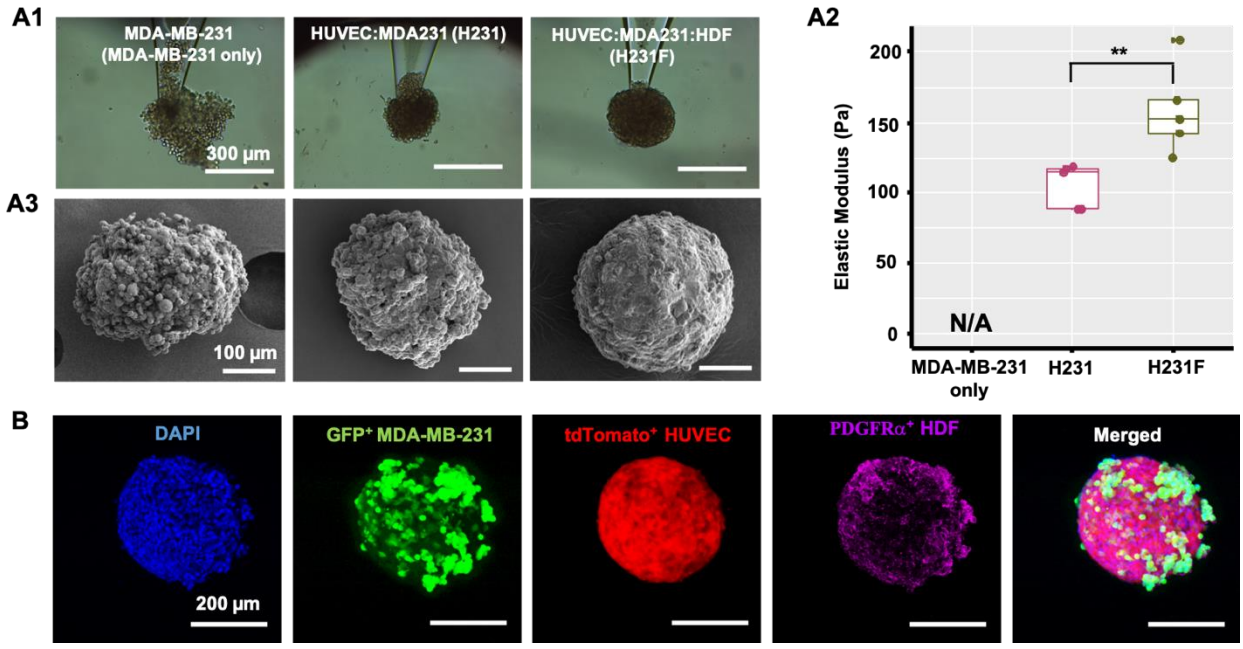

Figure S1: Evaluation of spheroid properties for aspiration-assisted bioprinting. Three different tumor spheroids were used to compare the mechanical and structural properties. Tumor spheroids used were spheroids formed by only MDA-MB-231 cells (MDA-MB-231-only), combination of HUVECs and MDA-MB-231s (H231) and combination of HUVECs, MDA-MB-231 and HDFs (H231F). (A1) Tumor spheroids were aspirated with a glass micropipette for 10 min to analyze their structural integrity under aspiration. (A2) Graphical representation of elastic modulus measured for the tumor spheroids (n=3 for all, $p^{***} < 0.001$, $p^{**} < 0.01$, $p^{*} < 0.5$). (A3) SEM images of tumor spheroids exhibiting distinctly different surface topographies. (B) Fluorescent images of the composite H231F tumor spheroids displaying all three different cell types, namely GFP^{+} MDA-MB-231 cells, $tdTomato^{+}$ HUVECs and $PDGFR\alpha^{+}$ HDFs. DAPI (blue) stained all cell nuclei.

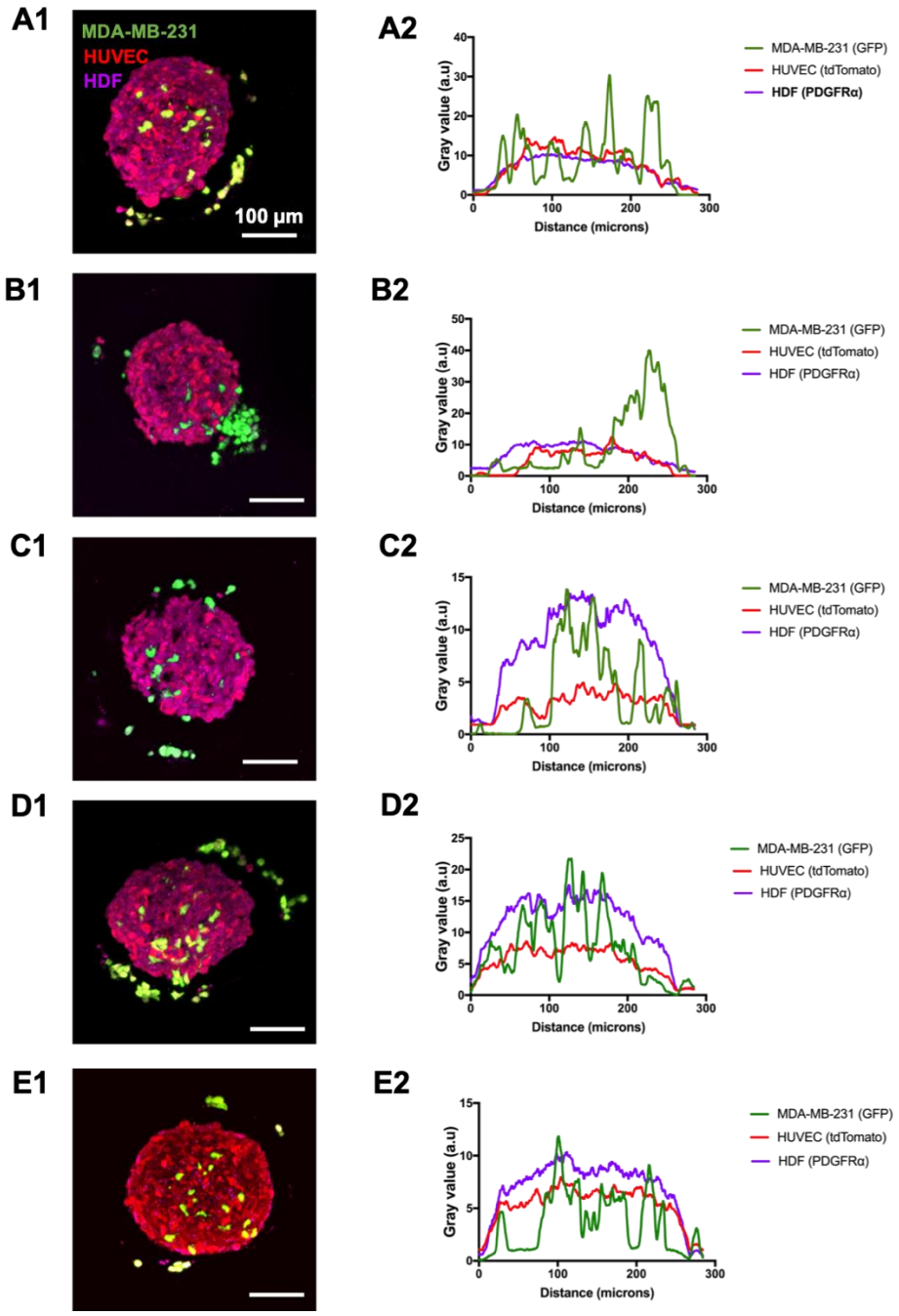

Figure S2: (A1-E1) Confocal images of five H231F tumor spheroid sections showing GFP^+ MDA-MB-231, $tdTomato^+$ HUVECs and PDGFRα stained HDFs. (A2-E3) Graphical representations of fluorescent profiles of the histological sections.

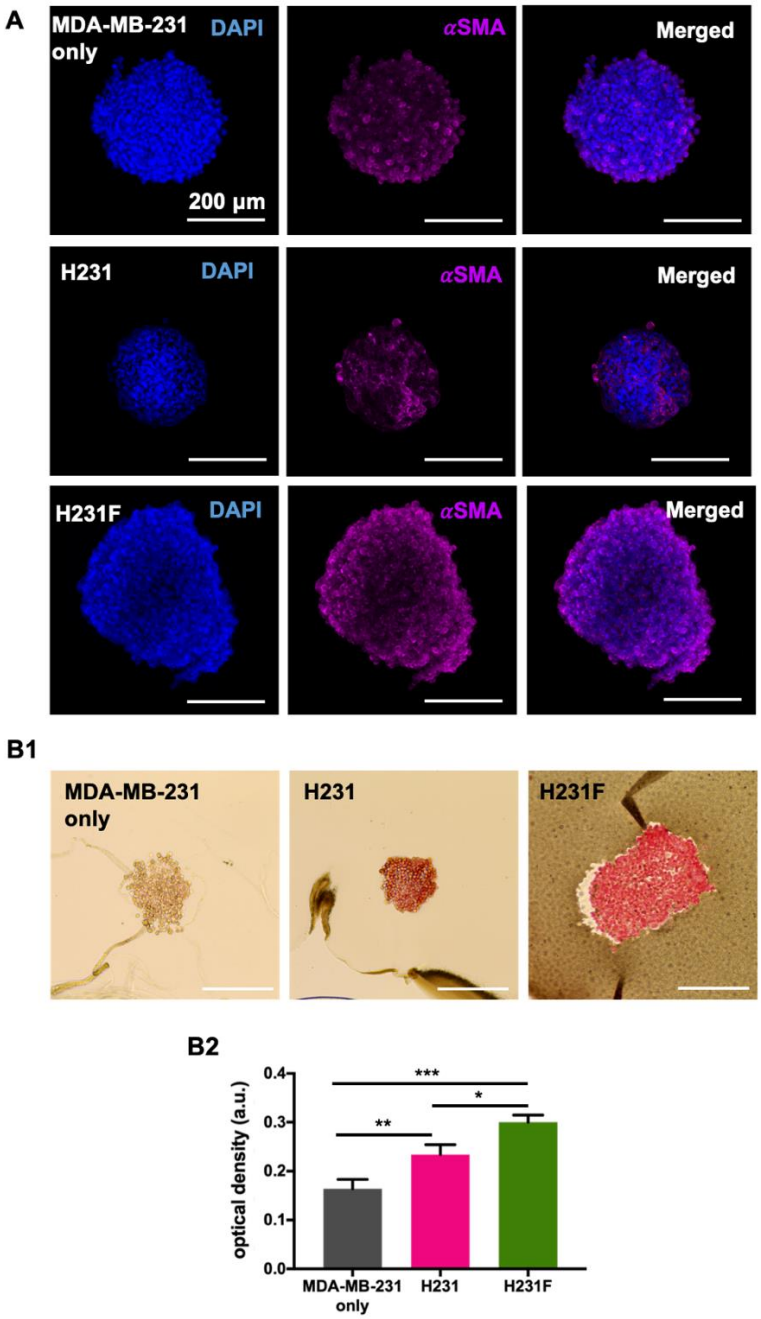

Figure S3: (A) Confocal images of MDA-MB-231 only, H231 and H231F tumor spheroids stained for αSMA and DAPI. (B1) Picrosirius red staining images of MDA-MB-231 only, H231 and H231F tumor spheroid histological sections. (B2) Graphical representation of optical density of picrosirius red stained MDA-MB-231-only, H231 and H231F tumor spheroids. (n=3, $p^{***} < 0.001$, $p^{**} < 0.01$, $p^{*} < 0.05$).

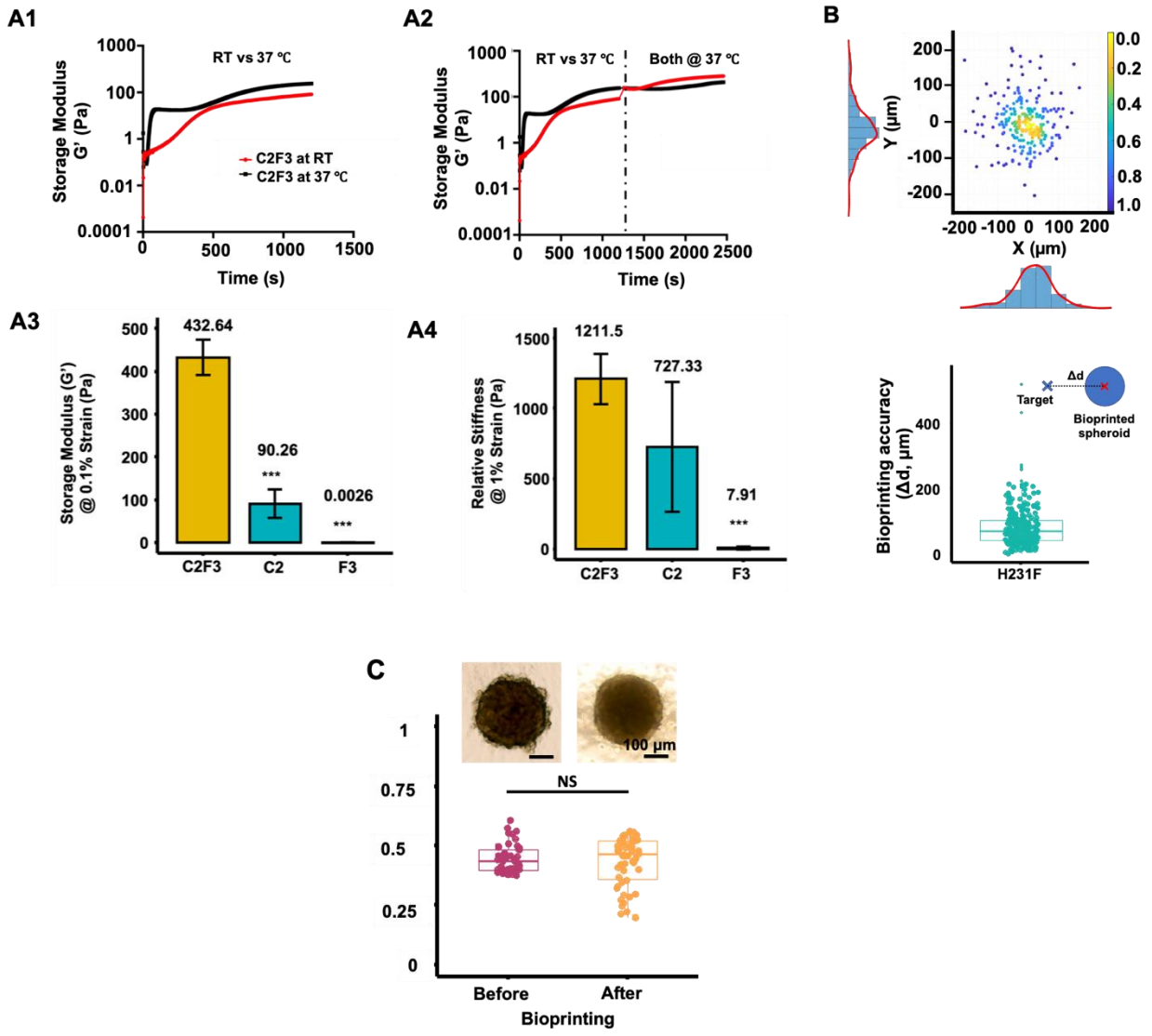

Figure S4: Evaluation of hydrogel properties for aspiration-assisted bioprinting. (A1) Graphical representation of change in storage modulus over time of the composite hydrogel (C2F3) incubated at room temperature (RT) and 37 °C for 20 min. (A2) Graphical representation of change in storage modulus over time for C2F3 incubated at RT and 37 °C for 20 min and then incubated at only 37 °C. (A3) Graphical representation of storage modulus for C2F3 versus its precursor, C2 and F3, all incubated at 37 °C for 40 min. (A4) Graphical representation of the relative stiffness of C2F3 as compared to its precursors, C2 and F3, all incubated at 37 °C for 40 min. (B) Graphical representation of bioprinting positional accuracy for spheroids bioprinted at

defined X, Y locations (graph on top) and a measured drift calculated between the target and actual location (bottom graph) (*n*=250). (C) Graphical representation of H231F tumor spheroid circularity measured before and after aspiration-assisted bioprinting (*n*=50, $p^{***} < 0.001$, $p^{**} < 0.01$, $p^{*} < 0.05$).

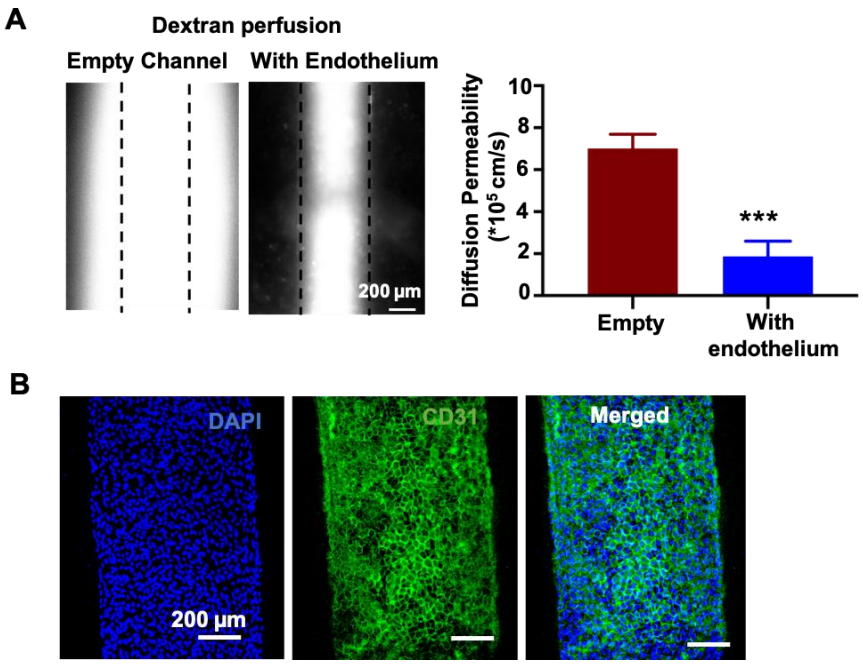

Figure S5: (A1) Fluorescent images of dextran perfusion in empty and endothelialized channels and their corresponding permeability values. (A2) Confocal images of endothelialized channels stained for CD31 and DAPI (4′,6-diamidino-2-phenylindole).

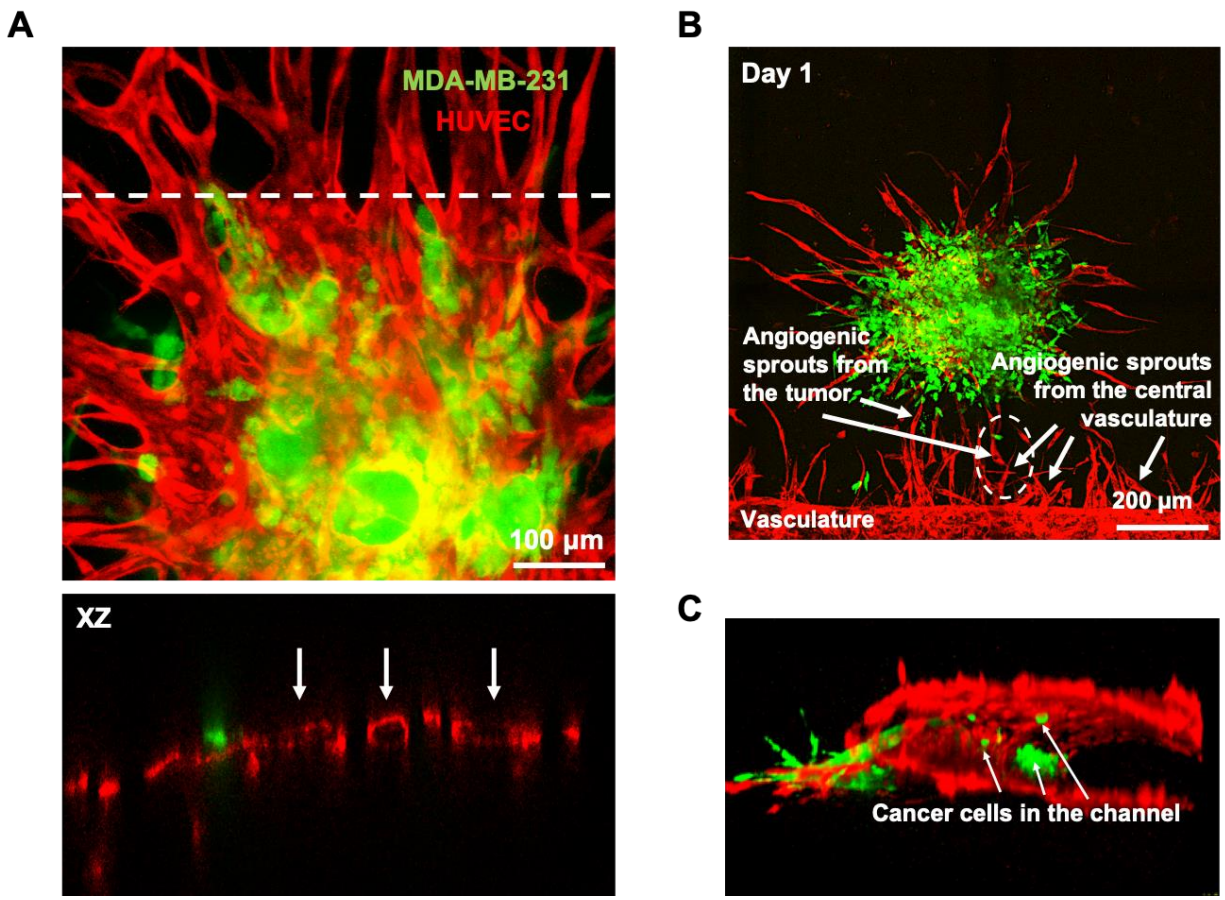

Figure S6: (A) An orthogonal projection across XZ plane revealing angiogenic sprouts containing hollow capillaries. White arrows are marked to represent the circular cross-section of vessels. (B) A multiphoton image showing angiogenic sprouts originating from the tumor and central vasculature. (C) 3D Reconstruction of the perfused central vasculature containing MDA-MB-231 cells. White arrows indicate MDA-MB-231 cells trying to invade into the vasculature.

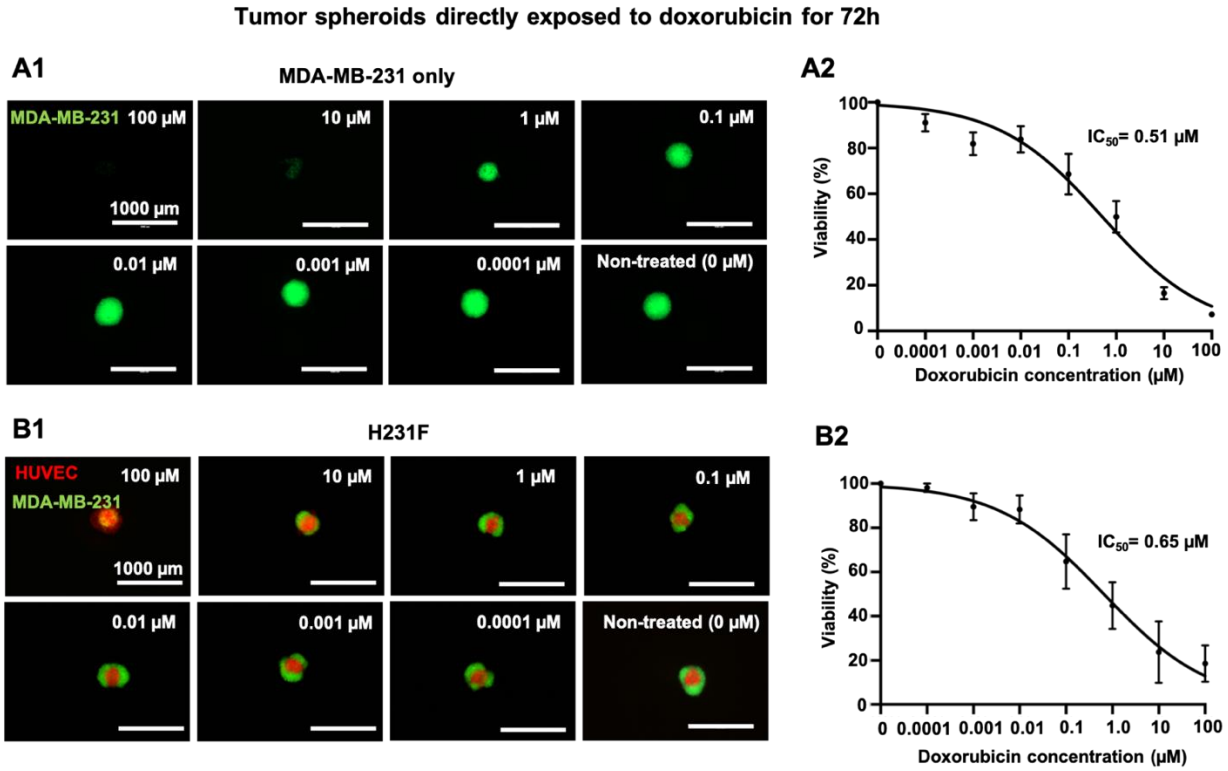

Figure S7: Exposure of free-standing tumor spheroids to doxorubicin. (A1) Fluorescent images of homocellular MDA-MB-231 tumor spheroids (MDA-MB-231-only) taken after 72 h of doxorubicin treatment. (A2) Dose-response curve for MDA-MB-231 spheroids treated with a range of 0 – 100 µM of doxorubicin concentration. (B1) Fluorescent images of co-cultured H231F tumor spheroids taken after 72 h of doxorubicin treatment. (B2) Dose-response curve H231F spheroids treated with a range of 0 – 100 µM doxorubicin concentration (n=3 for all).

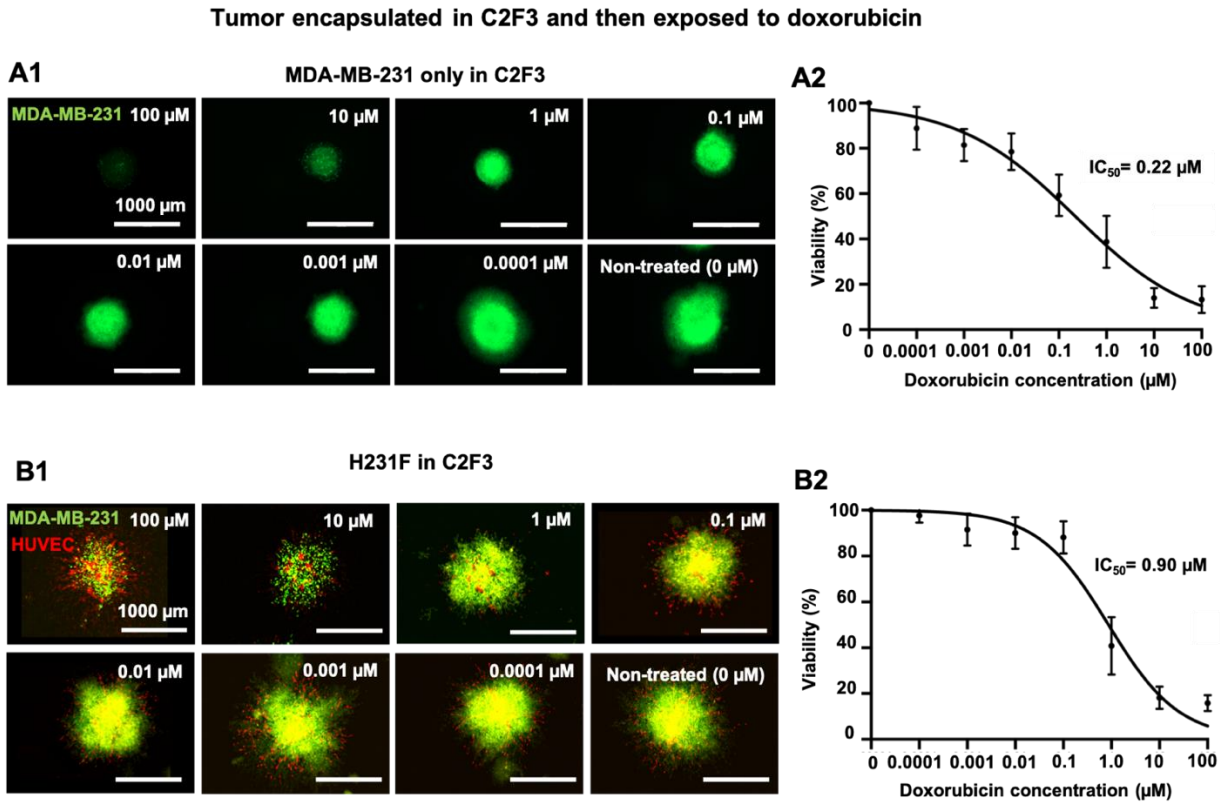

Figure S8: Exposure of hydrogel encapsulated tumor spheroids to doxorubicin. (A1) Fluorescent images of C2F3 encapsulated homocellular MDA-MB-231 spheroids after 72 h of doxorubicin treatment and (A2) the corresponding dose-response curve for MDA-MB-231 spheroids. (B1) Fluorescent images of C2F3 encapsulated co-cultured H231F spheroids after 72 h of doxorubicin treatment and (B2) the corresponding dose-response curve for H231F spheroids (*n*=3 for all).

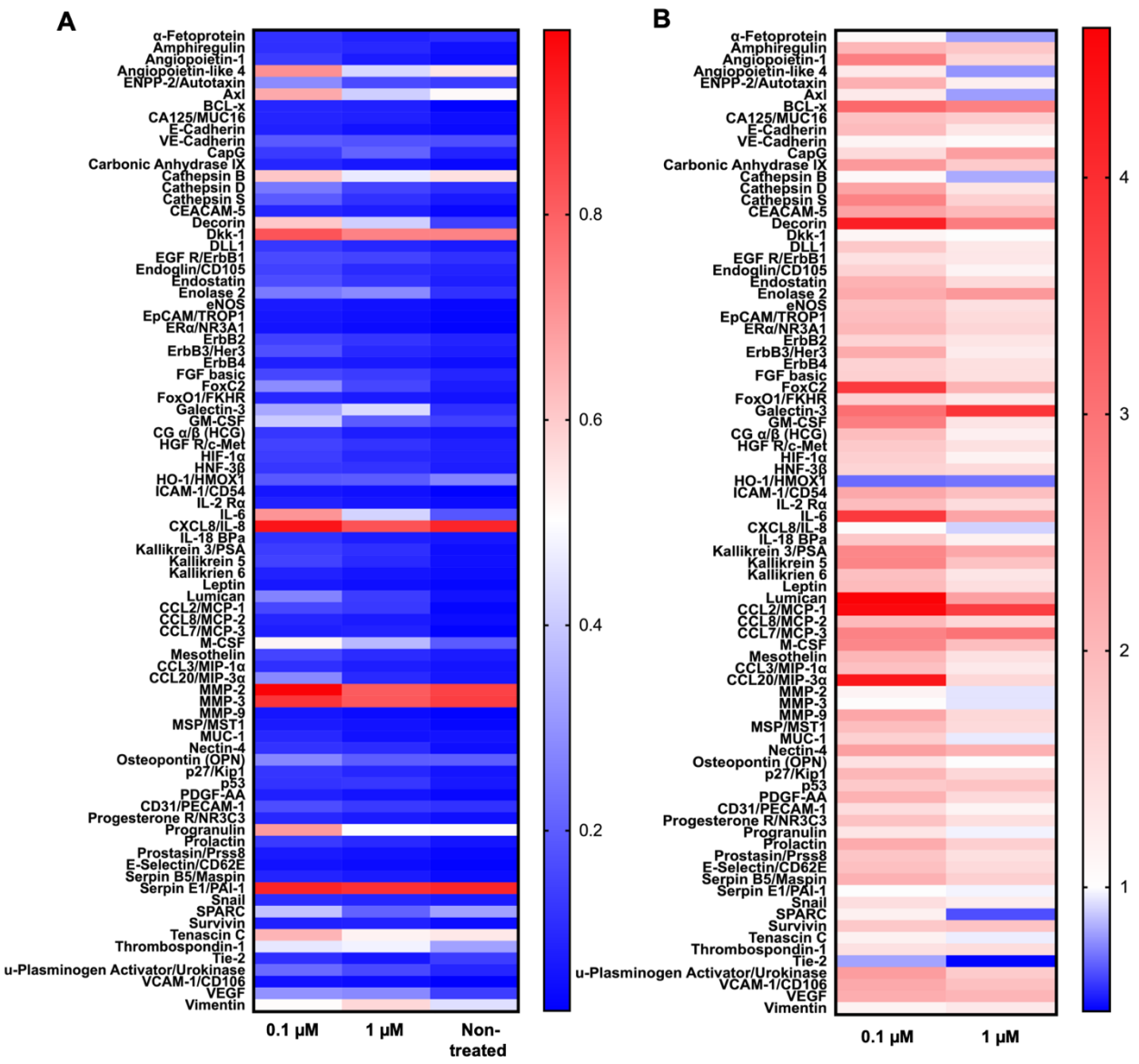

Figure S9: (A) Heatmap and (B) fold change in protein expression of 84 oncology-related proteins. Blue and red denoted the fold-change value lower and higher than the non-treated group, respectively. Non-treated group was normalized to 1 (*n*=3 for all).

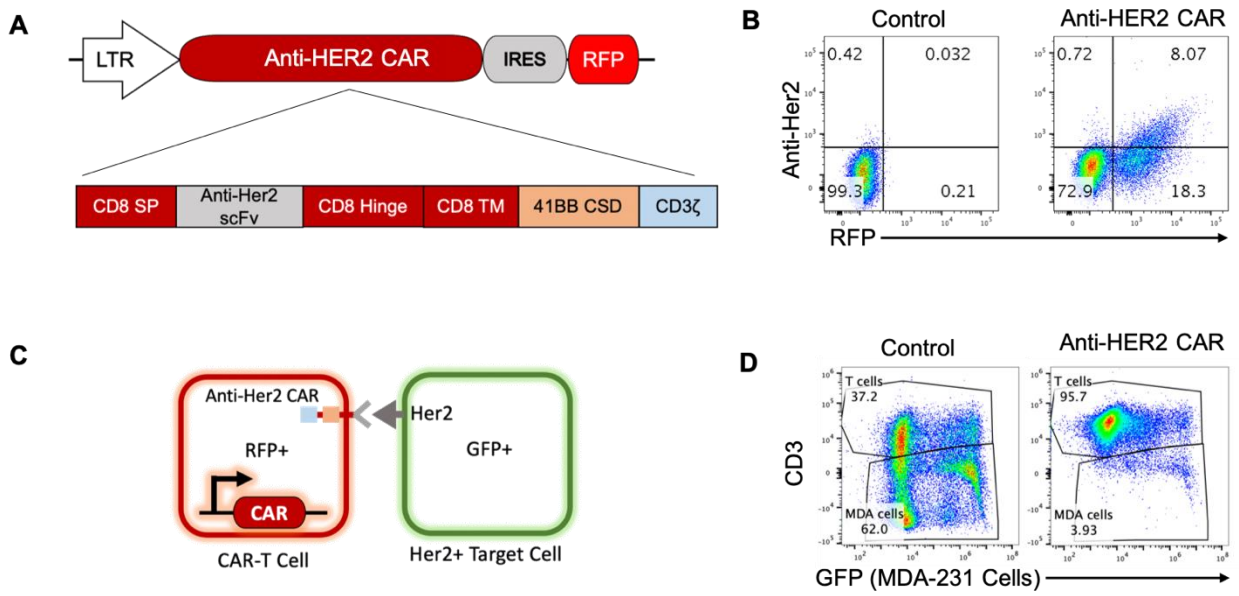

Figure S10: Development of HER2-specific CAR-T cells. (A) Constitutive LTR promoter drives the anti- HER2 CAR and RFP genes. Anti-HER2 CAR construct comprises CD8 alpha signal peptide (SP), single chain variable fragment (ScFv) of an anti-HER2 antibody, CD8 Hinge, CD8 transmembrane (TM) domain, 4-1BB (CD137) co-stimulatory domain (CSD) and CD3ζ (zeta) domain. (B) Expression of anti-HER2 ScFv on the surface of human T cells engineered with the anti-HER2 CAR construct. $CD8^+$ T cells were activated with anti-CD3/CD28 beads and transduced with a lentivirus encoding HER2-CAR and RFP then expanded for 10-12 days in IL-2 containing media and stained for expression of anti-HER-2 with a Her2-Fc recombinant protein followed by an anti-Fc antibody, as described in methods. The cells were then expanded in the culture in the presence of IL-2 for 10-12 days. (C) Cytotoxicity assay with anti-HER2 CAR-T effector cells (red) and $HER2^+$ target cells (green). Recognition of HER2 on the target cells triggers activation of T cells via the cytoplasmic domains of chimeric antigen receptor. Activation of the effector T cells then induces apoptosis of the $HER2^+$ target cells. (D) Cytotoxicity assay for anti-$HER2^+$ MDA-MB-231 cells. Human CD8 T cells transduced with an empty lentivector were used as controls. CD8 T cells were identified with CD3 staining and

target cells (MDA-MB-231) through expression of GFP. Effector (CAR expressing T cells) to target ratio of 1:1 is shown.

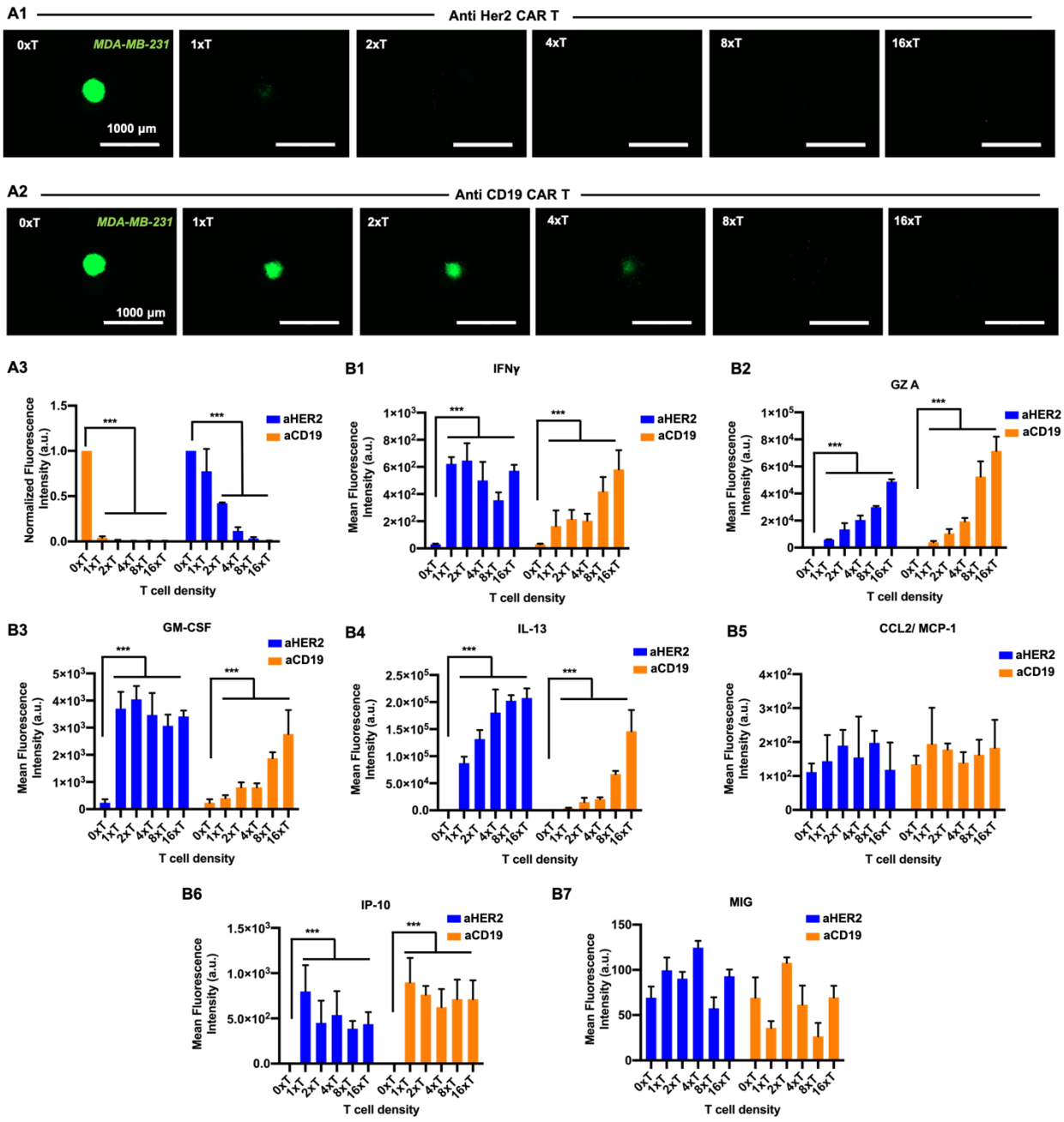

Figure S11: CAR-T cell therapy on *in vitro* static cultures of homotypic MDA-MB-231. CAR-T cell density was varied as 1xT (1:1), 2xT (2:1), 4xT (4:1), 8xT (8:1), 16xT (16:1). 0xT denotes the non-treated control culture. Fluorescent images of MDA-MB-231-only spheroids after 72 h of (A1) anti HER2 CAR-T cell and (A2) anti CD19 CAR-T cell treatment. (A3) Graphical representation of normalized fluorescence intensity of anti HER2 CAR-T cell and anti CD19

CAR-T cell treatment. Graphical representation of the mean fluorescence intensity of the cytokines and chemokines secreted after 72 h of CAR-T cell perfusion including (B1) IFNγ, (B2) Granzyme A, (B3) GM-CSF, (B4) IL-13, (B5) CCL2/ MCP-1, (B6) CXCL10/ IP-10, and (B7) MIG (*n*=3, $p^{*}<0.05$, $p^{**}<0.01$, $p^{***}<0.001$).

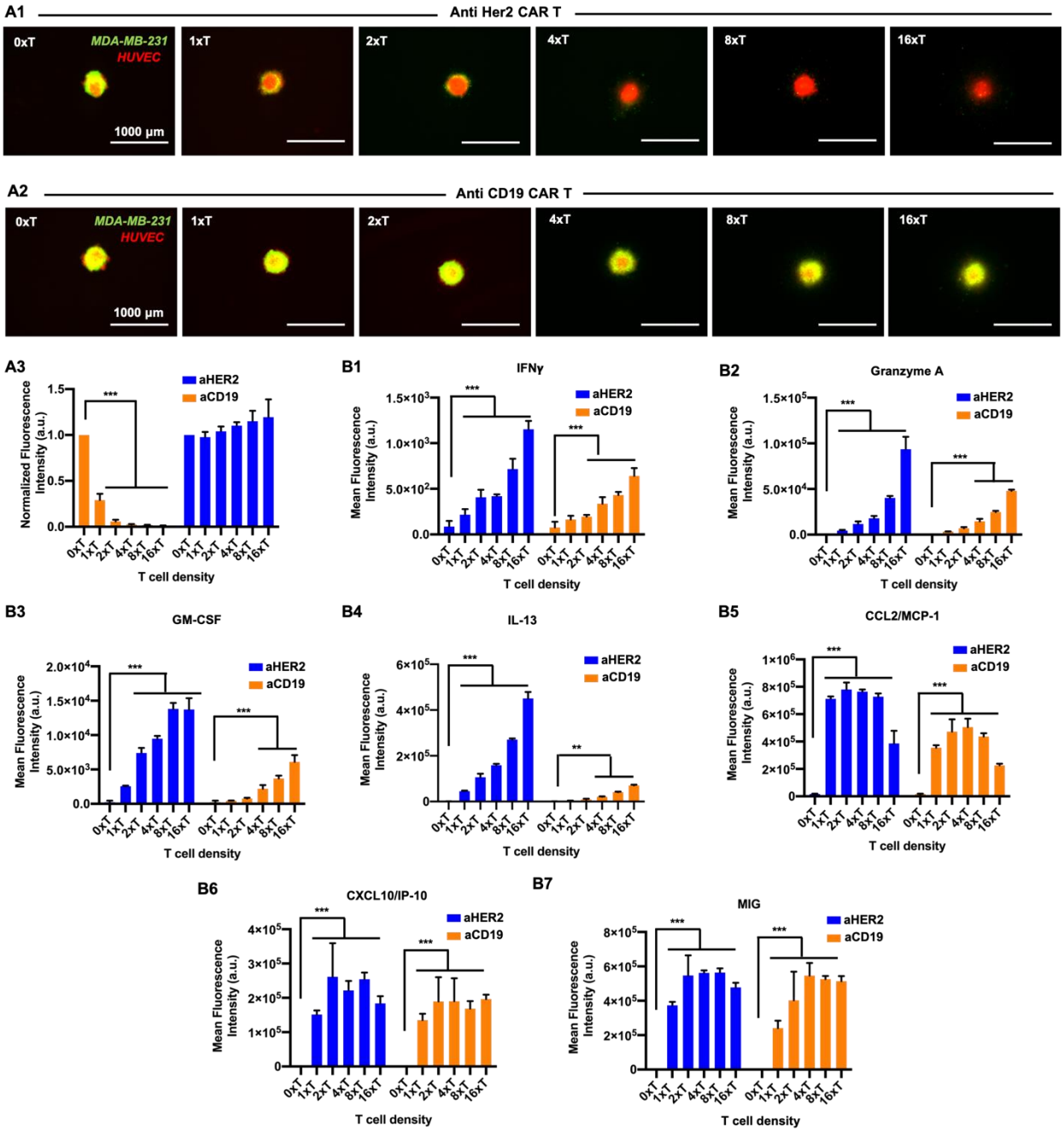

Figure S12: CAR-T cell immunotherapy on *in vitro* static cultures of heterotypic H231F tumors. CAR-T cell density was varied as 1xT (1:1), 2xT (2:1), 4xT (4:1), 8xT (8:1), 16xT (16:1). 0xT denotes the non-treated control culture. Fluorescent images of H231F tumors after 72 h of (A1) anti HER2 CAR-T cell and (A2) anti CD19 CAR-T cell treatment. (A3) Graphical representation of normalized fluorescence intensity of anti HER2 CAR-T cell and anti CD19 CAR-T cell

treatment. Graphical representation of the mean fluorescence intensity of the cytokines and chemokines secreted after 72 h of CAR-T cell perfusion including (B1) IFNγ, (B2) Granzyme A, (B3) GM-CSF, (B4) IL-13, (B5) CCL2/ MCP-1, (B6) CXCL10/ IP-10, and (B7) MIG (*n*=3, $p^{*}<0.05$, $p^{**}<0.01$, $p^{***}<0.001$).

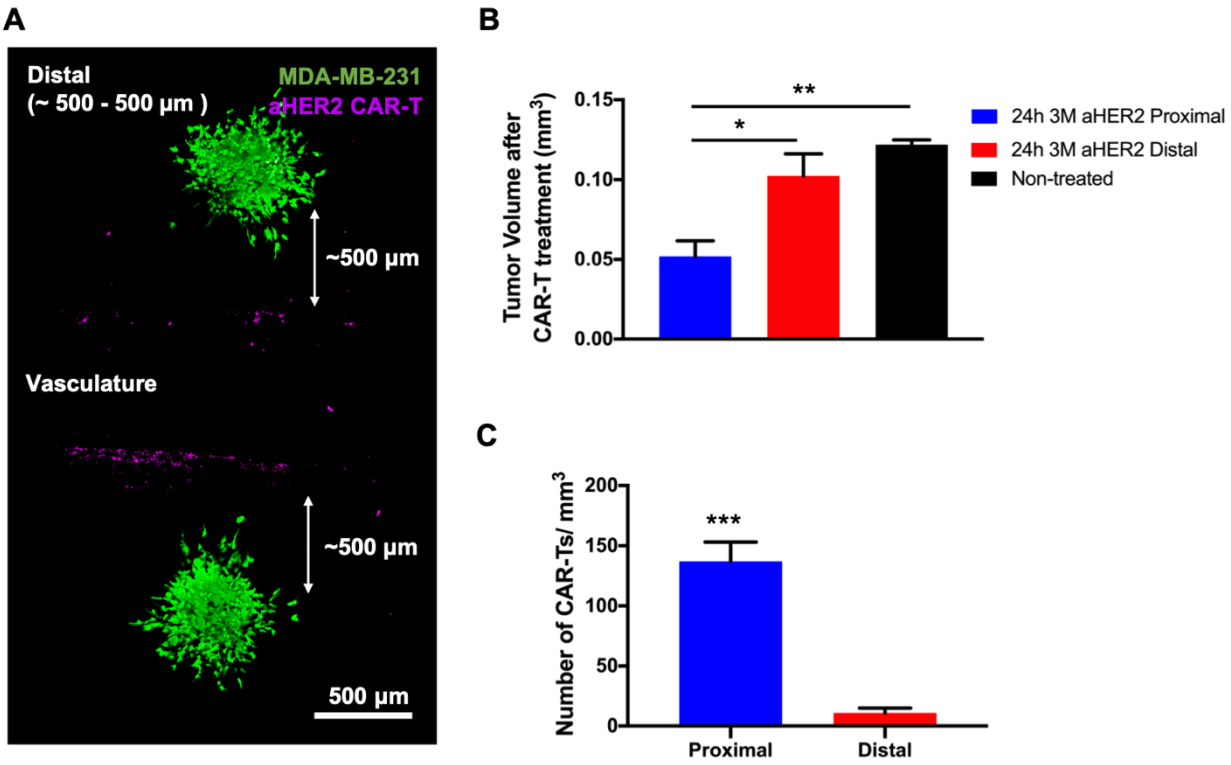

Figure S13: (A) A multiphoton image of distally bioprinted tumor spheroids treated with anti HER2 CAR-T cells showing CAR-Ts adhering to the vasculature. Graphical representation of (B) tumor volumes after CAR-T treatment and (C) number of CAR-T cells per mm^3 volume after 24h of anti HER2 CAR-T perfusion.

Supplementary Movies

Movie S1. Aspiration-assisted bioprinting of H231F tumors in a biomimetic C2F3 matrix.

Movie S2. 3D Reconstruction of the bioprinted perfusable tumor model illustrating the endothelialized vasculature and tumors (with angiogenic sprouting) bioprinted near the vasculature.

Movie S3. 3D Reconstruction of the endothelialized vasculature illustrating cancer cells trying to invade into the perfused vasculature.

Movie S4. CAR-T cells flowing through the endothelialized vasculature.

Movie S5. Confocal Z stacks of a H231F tumor spheroid.

References

[1] M. Dey, B. Ayan, M. Yurieva, D. Unutmaz, I. T. Ozbolat, *Adv. Biol.* **2021**, *2100090*, 1.